Marine Geology 390 (2017) 199–213

Contents lists available at ScienceDirect

Marine Geology

journal homepage: www.elsevier.com/locate/margo

Effect of sea level rise and tidal current variation on the long-term evolution of offshore tidal sand ridges

Bing Yuan*, Huib E. de Swart

Institute for Marine and Atmospheric Research Utrecht, Utrecht University, Princetonplein 5, Utrecht 3584CC, The Netherlands

ARTICLE INFO

Keywords:
Active sand ridges
Quasi-active/inactive sand ridges
Southern North Sea
Celtic Sea
Morphodynamic model

ABSTRACT

Tidal sand ridges are large-scale bedforms that occur in the offshore area of shelf seas. They evolve on a time scale of centuries due to tide-topography interactions while being further shaped by wind waves. During their evolution, ridges are also affected by changes in sea level, strength and direction of the tidal current. According to their present-day behavior, ridges are classified as 'active' (sand transport everywhere), 'quasi-active' (sand transport only on parts of the ridges) and 'inactive' (no sand transport anywhere). Using a nonlinear morphodynamic model, the present study extends earlier work by investigating the effect of sea level rise and changes in the amplitude and principal direction of the tidal current on the growth time and height of active tidal sand ridges. Besides, the role of sea level rise and tidal current variation in the presence of quasi-active/inactive ridges is explored. Two specific settings are considered, which are characteristic for the Dutch Banks in the North Sea and for sand ridges in the Celtic Sea. The time range considered here is less than 20,000 years, roughly the period from the Last Glacial Maximum to the present.

Generally active tidal sand ridges occur if the tidal current amplitude is larger than 0.5 m/s. For these ridges, with increasing rates of sea level rise, their growth time becomes longer, and the root mean square height keeps on increasing. A smaller initial tidal current amplitude gives rise to a larger growth time, while changes in the principal current direction have a minor effect on the characteristics of the ridges. On the considered time scale, assuming a constant wave climate, quasi-active tidal sand ridges occur mainly as a result of a decreasing tidal current amplitude such that the effective velocity (in the sense of stirring sand) becomes smaller than the critical velocity for sand erosion. The ridges further become inactive on a time scale that depends inversely on the rate of sea level rise. Modeled ridges are compared with observed ridges. Similarities are found and quantitative differences are explained.

1. Introduction

Tidal sand ridges are large-scale rhythmic sea bottom patterns with a typical spacing (distance between successive crests) of several kilometers and a height of tens of meters. Their crests are slightly cyclonically (5° –30°) oriented with respect to the principal direction of the tidal current. These ridges are observed in offshore areas of shelf seas (Off, 1963; Liu et al., 1998; Dyer and Huntley, 1999, and references therein) that have a wide range of water depths, for instance, the southern North Sea (20–40 m), the East China Sea (60–120 m) and the Celtic Sea (120–170 m). According to their present-day morphodynamic activity, ridges are classified as 'active', 'quasi-active' and 'inactive'. Active and inactive mean that sand transport is present and absent in the area where the ridges occur, and quasi-active means that sand is transported on only parts of the ridges. Generally, active ridges are found in relatively shallow waters (10–50 m) where strong tidal currents occur (above 0.5 m/s), e.g., in the southern North Sea (Kenyon et al., 1981). In contrast, inactive ridges are observed in relatively deep waters (100–200 m) where tidal currents are weak (maximum velocity is insufficient to move the sand near bed), e.g., in the Celtic Sea (Stride et al., 1982), or in areas with limited availability of sand. In shelf seas where the water depth and the current strength are between those for active and inactive ridges, such as the East China Sea (Liu et al., 2007), quasi-active ridges occur. Fig. 1 shows examples of tidal sand ridges in the Southern North Sea and the Celtic Sea. Acquiring more knowledge about the long-term dynamics of these ridges is desirable for practical issues, such as assessment of the stability of underwater structures and strategic planning of marine sand mining (van Lancker et al., 2010).

The initial formation of tidal sand ridges has been explained as the result of morphodynamic self-organization, which involves the interactions between the sandy bed and the tidal current (Huthnance, 1982a). Linear stability analysis yields a preferred bedform of which

* Corresponding author.
E-mail addresses: b.yuan@uu.nl (B. Yuan), H.E.deSwart@uu.nl (H.E. de Swart).

http://dx.doi.org/10.1016/j.margeo.2017.07.005
Received 4 April 2017; Received in revised form 26 June 2017; Accepted 5 July 2017
Available online 08 July 2017
0025-3227/

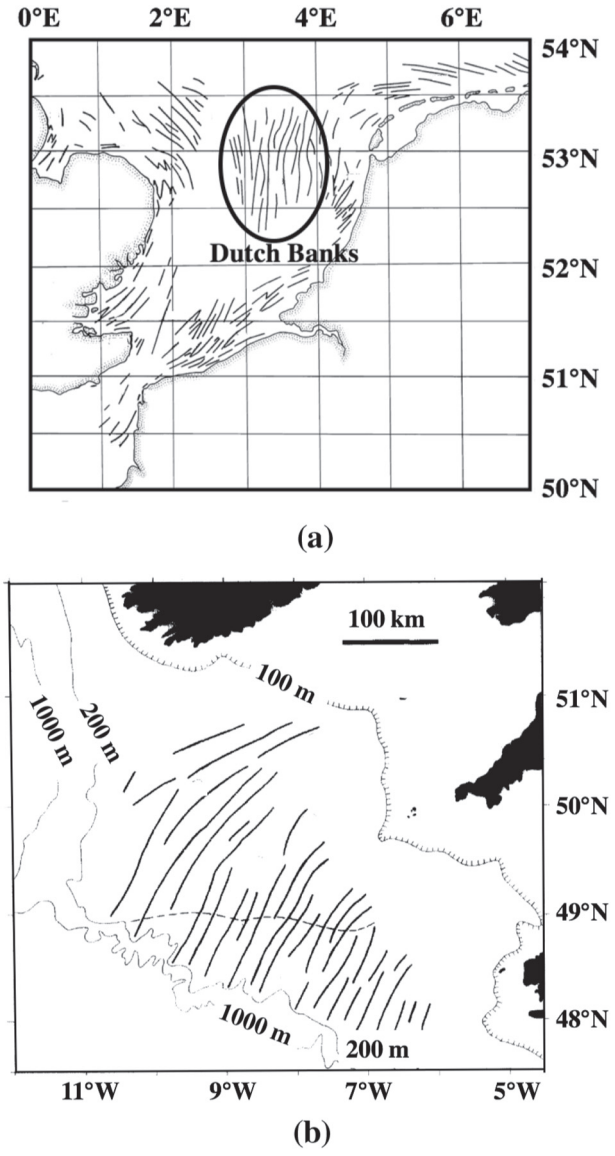

Fig. 1. Tidal sand ridges in (a) the southern North Sea (after Dyer and Huntley, 1999) and (b) the Celtic Sea (after Belderson et al., 1986).

the spacing and orientation are in fair agreement with those of the observed tidal sand ridges. For ridges with a finite height, nonlinear (or weakly nonlinear) models (Huthnance, 1982b; Roos et al., 2004; Tambroni and Blondeaux, 2008; Yuan et al., 2017, and references therein) were employed to investigate the behavior of these ridges. In these models, the sea level and the tidal current were kept constant in time.

However, tidal sand ridges evolve on a time scale of many hundreds of years, during which both the sea level and the characteristics of the tidal current change. For instance, Beets and van der Spek (2000) showed that the sea level for the continental shelves of Belgium and the Netherlands at 8 ka BP (8000 years before present) was about 15 m lower than the present sea level. Further earlier during the Last Glacial Maximum lowstand, the eustatic (opposed to local) sea level was 125 ± 5 m lower than that in the present day (Fleming et al., 1998). As the growth rate of the height of the ridges is comparable to the rate of sea level rise (SLR), it is evident that SLR plays a role in the long-term evolution of these ridges. It is suggested that quasi-active/inactive ridges were initially formed during a low sea level (e.g., ~ 20 ka BP for ridges in the Celtic Sea) and subsequently became less active or inactive as the sea level rose (Belderson et al., 1986; Yang, 1989). Regarding the tidal current, van der Molen and de Swart (2001) showed that large variation of tidal conditions occurs in the southern North Sea during the Holocene period. Uehara et al. (2006) modeled the evolution of the semidiurnal lunar M_2 tidal current in the northwest European shelf sea from the Last Glacial Maximum to the present, and significant changes in the amplitude of the modeled M_2 current were found in the Celtic Sea. Since the strength of the tidal current determines sand transport rate and the principal current direction affects the ridge orientation, variation in the strength and principal direction of the current also plays a role in the evolution of the ridges. Note that the wave climate (wave height and wave period) also changes on the considered time scale (see e.g. Neill et al., 2009). Huthnance (1982b) and Roos et al. (2004) showed that bed erosion due to wave stirring prevents the crests of the ridges from growing unrealistically close to the sea surface, as the near-bed wave orbital velocity is inversely proportional to the water depth.

Based on the considerations above, the aims in this study are two-fold. First, to quantify the effect of SLR and variation in the strength and principal direction of the tidal current on the characteristics (growth time and height) of active tidal sand ridges. Second, to explore the role of SLR and tidal current variation in the occurrence of quasi-active/inactive ridges. Note that the time scale considered is of order 10 ka, which represents that for the ridges in the southern North Sea and the Celtic Sea. The reason to choose these areas is that they are two of the world's largest systems of tidal sand ridges, and ridges in these areas are representative for active and inactive ridges according to the previous studies. Besides, for these areas studies of reconstructed sea level curve and simulated tides and waves from the Last Glacial Maximum lowstand until present are available, which provide the conditions of sea level, tides and waves for the present model input. Changes in the wave height and wave period are not investigated here, and unlimited availability of sand in the bed is assumed.

To fulfill these aims, an extended version of the idealized nonlinear morphodynamic model in Yuan et al. (2017), originally developed by Caballeria et al. (2002) and Garnier et al. (2006) to study sand bars in the nearshore zone, was used. The extension concerns the consideration of SLR and tidal current variation. The model describes the feedbacks between tidally forced depth-averaged currents and the sandy bed on the outer shelf, and following Huthnance (1982b) and Roos et al. (2004), the stirring of sand by wind waves is accounted for in the formulation for sand transport. The approach to include SLR resembles that of Nnafie et al. (2014), who studied the influence of SLR on dynamics of shoreface-connected sand ridges, which are large-scale bedforms observed on inner shelves. In that study, it was demonstrated that SLR is a key factor for the dynamics of those ridges. Compared to the previous models (Caballeria et al., 2002; Garnier et al., 2006; Nnafie et al., 2014), in the present model and in Yuan et al. (2017), different aspects are considered: an open domain with periodic boundary conditions in both horizontal directions instead of semi-infinite domain that is bounded by a coast, a flat bottom instead of a sloping bottom, tidal currents instead of wind- and wave-driven currents, and tidally-averaged sand transport instead of wave-averaged sand transport.

The manuscript is organized as follows. In Section 2, the morphodynamic model is briefly introduced, followed by a description of quantities for the characteristics of finite-height ridges and experiments design. Two specific default settings are considered, which are representative for the Dutch Banks in the southern North Sea and for ridges in the Celtic Sea. Results are presented in Section 3 and subsequently discussed in Section 4. Finally, Section 5 contains the conclusions.

2. Material and methods

2.1. Model

An open domain is considered to mimic offshore areas where tidal

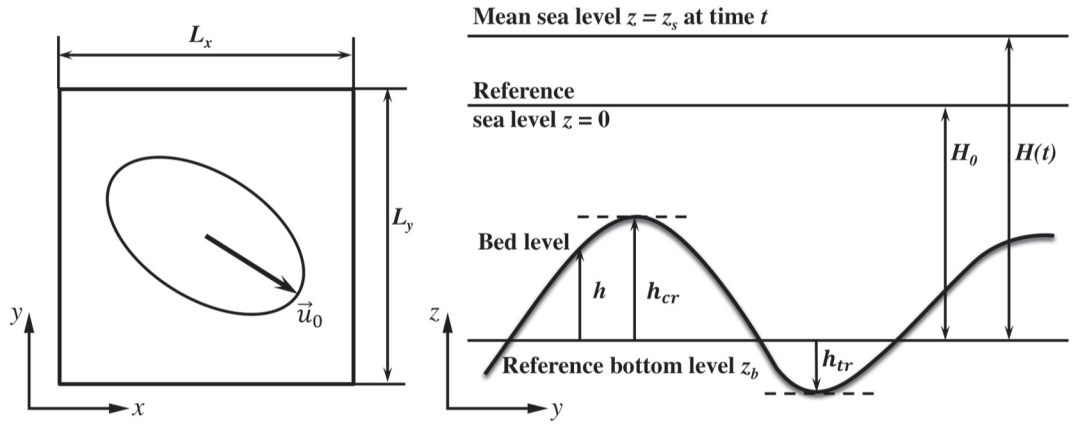

Fig. 2. Top view (left) and side view (right) of the model geometry. In the top view, the tidal ellipse of the background current $\vec{u}_0$ is shown. In the side view, the bed level h with respect to the reference bottom level z_b, the reference sea level $z = 0$ (initial mean sea level), the time-varying mean sea level $z = z_s$, the initially undisturbed water depth H_0, and the crest and trough levels h_{cr} and h_{tr} with respect to z_b are also shown.

sand ridges are usually observed. Cartesian coordinates x, y and z are used. In the presence of bedforms, the current is modeled by the depth-averaged shallow water equations (see details in Appendix A). This means that the vertical structure of the flow is neglected, and consequently bedforms with small length scales (less than around 1 km) such as sand waves (Besio et al., 2006, and references therein) are not resolved. Periodic boundary conditions in both horizontal directions and a spatially uniform time-varying horizontal pressure gradient force $\vec{F_p}$ are imposed. This is justified by the assumption that the sizes of the domain (L_x and L_y in the x- and y-directions, respectively), which are in the order of the spacing between these ridges, are much smaller than the wavelength of the principal tidal wave. The force $\vec{F_p}$ is such that, in the absence of bottom undulations, it drives a spatially uniform background depth-averaged tidal current $\vec{u}_0$. The tidal constituent included in $\vec{u}_0$ has a velocity vector of which the end point follows an ellipse in a tidal period (referred to as tidal ellipse).

Mass conservation of sand determines the bed level evolution,

$$(1-p)\frac{\partial h}{\partial t} + \nabla\cdot<\vec{q}> = 0, \tag{1}$$

where h is the bed level with respect to the reference bottom level (see Fig. 2), t is time and $\langle\cdot\rangle = T^{-1}\int_0^T \cdot\, dt$ means tidal average, with T the tidal period. Furthermore, $\vec{q}$ is the volumetric sand transport per unit width, and p is the bed porosity. The evolution of the bedforms is to a good approximation related to the divergence of net sand transport averaged over a tidal cycle, as the time scale of tidal sand ridges (order of 100 years) is much larger than that of tides (order of 1 day). To calculate $\vec{q}$, a bed load formulation is used, which is modified after Fredsøe and Deigaard (1992) by considering an effective velocity in the sense of stirring sand:

$$\vec{q} = \alpha_e(u_e^2 - U_c^2)(1 - 0.7U_c/u_e)(\vec{u} - \Lambda u_e \nabla h)\mathscr{H}(u_e - U_c). \tag{2}$$

Here, α_e is the sand transport coefficient, Λ is a bed slope coefficient, and $\mathscr{H}$ is the Heaviside function. Furthermore, U_c is the critical depth-averaged velocity for sand erosion, and u_e is the effective velocity given by $u_e = (|\vec{u}|^2 + 0.5u_w^2)^{1/2}$ (Roos et al., 2004). Here, u_e^2 represents the wave averaged intensity of the flow, $\vec{u}$ is the velocity vector of the tidal current, and u_w is the amplitude of the depth-dependent wave-induced near-bed orbital velocity. Note that in other studies (see e.g. Soulsby, 1997), instead of the coefficient 0.5 in front of u_w^2, different values are used. Expressions for α_e, U_c and u_w are shown in Appendix B. Both α_e and U_c depend on water depth H and grain size d, and u_w is parameterized as a function of the wave height, wave period and the water depth. Note that as the water depth increases, U_c increases while u_w decreases, as can be seen from Eqs. (13)–(14) and (16) in Appendix B.

SLR is included in the model by considering changes in the mean sea level z_s with a rate of R but no change in the mean sea bottom level z_b (see Fig. 2), i.e.,

$$\frac{dz_b}{dt} = 0, \qquad \frac{dz_s}{dt} = \frac{dH}{dt} = R. \tag{3}$$

This means that the change in the mean water depth $H = z_s - z_b$ due to isostatic rebound (see e.g. Lambeck, 1995) is not taken into account, but it can be mimicked by adjustment of the value of R in the model. The rate R of SLR is assumed to be a piecewise linear function of time. Similarly, changes in the tidal current characteristics are considered by assuming the velocity amplitude and the principal direction of $\vec{u}_0$ to be piecewise linear in time. By choosing the sea level and tidal conditions at several time spots from reconstructed sea level curves (e.g. Behre, 2007) and tidal conditions (e.g. Uehara et al., 2006) and applying the above assumptions, the general characteristics of the sea level and the tidal current are captured. The numerical scheme for the system is described in Appendix C.

2.2. Quantities to describe characteristics of finite-height bedforms

Following Garnier et al. (2006), a global growth rate Γ of the bedforms is employed to describe the growth or decay of the amplitude of the bedforms, which reads

$$\Gamma = \frac{1}{(h_{rms}^2)}\frac{\partial}{\partial t}\left(\frac{1}{2}h_{rms}^2\right). \tag{4}$$

Here, $h_{rms} = (\overline{h^2})^{\frac{1}{2}}$ is the root mean square height of the bedforms that indicates the variance of the bed level, with the overbar denoting spatial averaging.

Linear stability theory (Huthnance, 1982a) shows that initially the amplitudes of the bottom modes (Fourier modes of bottom perturbations) evolve exponentially in time. After the exponential growth stage, for a constant sea level and a constant tide and wave climate, the ridges reach a static equilibrium (Roos et al., 2004) or a dynamic equilibrium (Yuan et al., 2017), i.e., Γ becomes 0 or oscillates around 0 in time. Based on these studies, for a changing sea level and tidal condition, a global growth time τ_g is defined as the time when Γ becomes no more than 1% of the maximum value of Γ after the exponential growth stage. The quantity τ_g is meant to identify the end of the exponential growth stage of the ridges.

Furthermore, to characterize the height of the ridges, following Roos et al. (2004), the relative ridge height is used, which is the percentage of the maximum water depth (neglecting surface elevation) that the ridge height makes up in a cross-sectional (normal to crests) ridge profile:

Table 1
Values of rate R of SLR, initially undisturbed mean water depth H_0, velocity amplitude U and change $\Delta\varphi$ in the principal direction of the background tidal current for the Dutch Banks (Exps. 1–4) and the Celtic Banks (Exps. 5–9).

Exp. no.	R (mm/yr)	H_0 (m)	U (m/s)	$\Delta\varphi$ (°)
1	0, 0.5, 1.0, 1.5, 1.875, 2.5, 3.0	30	0.75	0
2	0.5, 1.0, 1.5, 1.875, 2.5, 3.0	10, 15, 20	0.75	0
3	1.875	15	0 ka: 0.50 2–∞ ka: 0.75 0.5	0
4	1.875	15	0 ka: 0.50 2–∞ ka: 0.75	0–2 ka: 15 2–∞ ka: 0
5	0–3 ka: 5.0 3–12 ka: 10.0 12–14 ka: 7.0 14–∞ ka: 1.0	15	0–8 ka: 8 0 ka: 1.25 8–10 ka: 0.75 12–∞ ka: 0.35	0–8 ka: 8 8–10 ka: 0 10–12 ka: 2 12–∞ ka: 0
6	1, 6.25	As Exp. 5	As Exp. 5	As Exp. 5
7	As Exp. 5	10, 20	As Exp. 5	As Exp. 5
8	As Exp. 5	As Exp. 5	0.67	As Exp. 5
9	As Exp. 5	As Exp. 5	As Exp. 5	0

If no time is specified, the values of the parameters are constant in time, 'ka' represents 1000 years, 0 ka corresponds to the starting time of simulation, and '–∞' means to the end of simulation.

$$h_{rel} = \frac{h_{cr} - h_{tr}}{H - h_{tr}}. \tag{5}$$

Here, $(h_{cr} - h_{tr})$ is the vertical distance between the crest and trough levels from the cross-sectional ridge profile, which represents the height of the ridge, with h_{tr} and h_{cr} being the trough and crest levels with respect to the fixed reference bottom level z_b (see Fig. 2).

2.3. Design of the experiments

To achieve the aims of this study, tidal sand ridges in the southern North Sea, specifically the Dutch Banks, are selected as a prototype of active sand ridges, while those in the Celtic Sea (Celtic Banks) are chosen to represent inactive ridges. The default parameter values are given in Table 2 in Appendix C. Full information about tidal constituents during the Holocene or earlier is lacking, hence only the semidiurnal M_2 tide is considered. This implies that the modeled bedforms have symmetrical cross-crest profiles and they do not migrate (Huthnance, 1982a; Roos et al., 2004; Yuan et al., 2017). Table 1 lists the experiments with different rates R of SLR, initially undisturbed water depth H_0, velocity amplitude U and change $\Delta\varphi$ in the principal direction of the background tidal current $\vec{u}_0$ for the Dutch Banks and the Celtic Banks. Positive $\Delta\varphi$ means that the major axis of tidal ellipses rotates counterclockwise.

For the Dutch Banks, in Exp. 1, different rates of SLR are considered and the background tidal current $\vec{u}_0$ is kept fixed. The initially undisturbed water depth H_0 and the velocity amplitude U of $\vec{u}_0$ are based on the present-day values. Constant rates R are used, which are chosen such that their values are below the maximum R based on the sea level curve from 8 ka BP of the southern North Sea (Behre, 2007), i.e., 8–7 ka BP: ~ 5 mm/yr, 7–5 ka BP: ~ 2.5 mm/yr, 5 ka BP to the present: ~ 1 mm/yr. Note that a constant rate of SLR of 1.875 mm/yr corresponds to an increase of 15 m in the water depth in a period of 8 ka, which mimics the overall change of the sea level during the last 8 ka in the southern North Sea.

In Exp. 2, different initially undisturbed water depths H_0 are considered together with constant rates of SLR. The depth $H_0 = 15$ m corresponds to the mean water depth at 8 ka BP in the southern North Sea. As sand ridges may start growing for different H_0 and the water depth is not constant in the entire southern North Sea, different values of H_0 (10, 20 m) from 15 m are considered, and the choice of H_0 is further

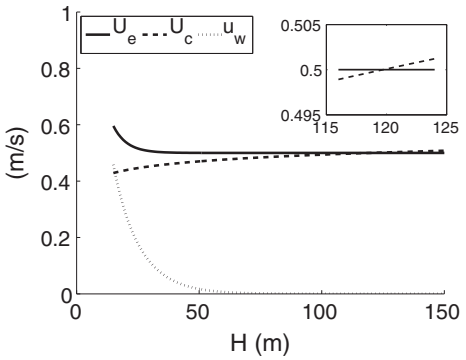

Fig. 3. The amplitude U_e of the effective velocity (solid line), the critical velocity for sand erosion U_c (dashed line) and the amplitude of near-bed wave orbital velocity u_w (dotted line) as a function of mean water depth H for the settings of the Dutch Banks with $U = 0.5$ m/s. Insert: zoom in for H between 115 m and 125 m.

discussed later in this section. Furthermore, in Exp. 3 changes in the background tidal current amplitude U are included, which are derived from the model results in Uehara et al. (2006). For comparison, a constant $U = 0.5$ m/s (representing the tidal condition at 8 ka BP in the southern North Sea) in time is also used. In Exp. 4 changes $\Delta\varphi$ in the principal current direction are considered, the values of which are obtained from modeled tidal ellipses from 7.5 ka BP to the present in the southern North Sea (van der Molen and de Swart, 2001). In all the experiments, the ellipticity ϵ of the tidal ellipse (ratio between the minor and major axes of the tidal ellipse) is assumed to be constant in time ($\epsilon = -0.2$), which is justified by the comparison between the modeled tidal ellipses at 7.5 ka BP and at present in the southern North Sea. A negative value of ϵ means that the current velocity vector rotates in a clockwise sense.

From Neill et al. (2009), the representative wave height and wave period are chosen to be $H_w = 2.5$ m and $T_w = 6$ s. Fig. 3 shows the calculated amplitude U_e of the effective velocity, the critical velocity for sand erosion U_c and the amplitude of near-bed wave orbital velocity u_w as a function of mean water depth H, where $U = 0.5$ m/s and other parameter values are representative for the case of the Dutch Banks. For the considered time range and rates of SLR, the mean water depth is less than 100 m, in which U_e is always larger than U_c. Note that for water depths close to 0, as the depth decreases the wave height and wave period decrease (Young and Verhagen, 1996), and so does the amplitude of the tidal current. If that is accounted for, the solid curve for U_e in Fig. 3 will go down as H (close to 0) decreases and it will intersect the dashed curve for U_c. The intersection point gives a critical minimum depth H_{0c} below which no tidal sand ridges will form. Here, the interest is in the cases that initially the sandy bed is active, thus the chosen initial water depth H_0 is always larger than H_{0c}. It is shown in Appendix D that by assuming a constant pressure gradient force $\vec{F_p}$ in time for small water depths, for $H = 15$ m, $U = 0.5$ m/s, $\epsilon = -0.2$ (Exp. 4) and the wind conditions in the considered regions, $H_{0c} \sim 10$ m. Furthermore, to a good approximation, H_w and T_w are kept constant for $H \geq H_{0c}$.

In the experiments for the Dutch Banks, the domain length and the initial principal direction of $\vec{u}_0$ are chosen based on the initially preferred bedform under the present-day conditions obtained from linear stability analysis. The initially preferred bedform under the present-day conditions has a spacing λ_p of 7.5 km, which is in the range of the present-day values (5.7–9.8 km from Roos et al., 2004), and its crests are 37° cyclonically oriented with respect to the principal current direction. Accordingly, the domain length in the y-direction L_y is chosen to be 7.5 km, and initially the major axis of $\vec{u}_0$ is 37° anticyclonically rotated with respect to the x-axis. In the default setting, the domain length L_x is chosen equal to L_y. The sensitivity of the results to L_x and L_y is discussed in Section 4.3.

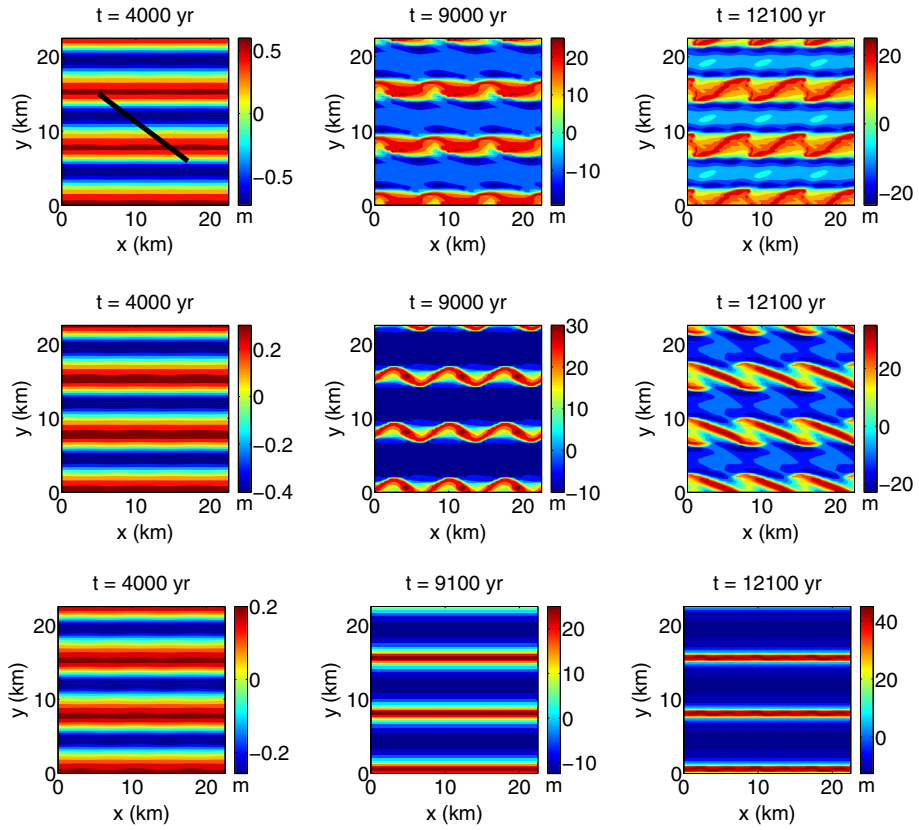

Fig. 4. Snapshots of bed level h at different times for different rates R of SLR with an initially undisturbed water depth $H_0 = 30$ m and $U = 0.75$ m/s (Exp. 1). From top to bottom panels, $R = 0$, 1 and 1.875 mm/yr, respectively. The bed level obtained in the domain of 7.5 km × 7.5 km is used to cover a domain with a size 3 × 3 times larger. The black line indicates the principal direction of the background tidal current $\vec{u}_0$. (For interpretation of the references to color in this figure legend, the reader is referred to the web version of this article.)

Regarding the Celtic Banks, the consensus is that their formation started at the Last Glacial Maximum lowstand, i.e, roughly at the time 20 ka BP (Scourse et al., 2009, and references therein). Several experiments using the conditions that mimic those for the Celtic Banks are conducted to investigate the role of SLR and tidal current variation on the occurrence of quasi-active/inactive ridges.

In Exp. 5 (see Table 1), both SLR and changes in the strength and principal direction of the tidal current are considered. The rate R of SLR in the Celtic Sea is adopted from Fleming et al. (1998) and Shennan et al. (2006), and in total the water depth increases by 125 m in 20 ka. The background tidal current amplitude U is based on the results of Uehara et al. (2006) (contours of U at 16, 12, 10, 8, and 0 ka BP in the northwest European shelf seas were shown). A linear trend of U during 20–12 ka BP is assumed to obtain U at 20 ka BP. The ellipticity ($\epsilon = -0.4$) and the change in the principal current direction are based on the model results in Belderson et al. (1986). An initially undisturbed water depth of 15 m is used. The representative wave height and wave period are chosen to be $H_w = 3$ m and $T_w = 7$ s according to the findings in Neill et al. (2009).

The possible occurrence of quasi-active/inactive ridges for different values of R, H_0, U and $\Delta\varphi$ is examined in Exps. 6–9. In Exp. 6, $R = 1$ mm/yr represents the present-day condition (Shennan et al., 2006), and $R = 6.25$ mm/yr is the average rate of SLR for an increase of 125 m of water depth in 20 ka. In Exp. 7, different values of H_0 are used, and the choice of the values follows from the same argument (critical initial water depth) for the Dutch Banks. Exp. 8 uses a constant value of U (0.67 m/s) in time, which is the time-averaged velocity amplitude in Exp. 5. Finally, Exp. 9 neglects changes in the principal current direction.

For the Celtic Banks, the domain length L_y is chosen to be close to the observed spacing of the Celtic Banks at present, i.e., 15 km, which is approximately three times of the wavelength of the initially preferred bedform in Exp. 5. The principal current direction (37° anticyclonically rotated with respect to the x-axis) is chosen such that the crest lines of the initially preferred bedform in Exp. 5 are parallel to the x-axis. The focus here is to gain insight into why active ridges become quasi-active/inactive, rather than to investigate the characteristics of quasi-active/inactive ridges in detail. For this reason, and because 2D (topography varies in both x- and y-directions) computations are very demanding in time, a 1D configuration (topography varies only in the y-direction) is employed. In all experiments, initially a random perturbation with a height of several centimeters in the domain is applied.

3. Results

3.1. Active ridges subject to SLR only: sensitivity behavior to R

Fig. 4 shows snapshots of the bed level at different times for different rates R of SLR with an undisturbed water depth H_0 of 30 m (Exp. 1). Spatially meandering crests are found in the case that SLR and tidal current variation are not considered (top panels). For relatively small rates of SLR of 1 mm/yr (middle panels), 0.5 mm/yr and 1.5 mm/yr (not shown), meandering crests still occur, but in the end the crests break (from one crest into two) and become stationary, and they are rotated with respect to the x-axis and become almost straight. Moreover, the spacing of the ridges decreases. In contrast, non-rotated straight crests parallel to the x-axis are observed for $R = 1.875$ mm/yr (bottom panels) and $R = 2.5$, 3 mm/yr (not shown) during the entire simulation period. The reasons for the presence of meandering crests, rotated and non-rotated straight crests in the end state are discussed in Section 4.1.

In Fig. 5, the time evolution of the bed level along a transect in the y-direction is shown for different rates R of SLR with $H_0 = 30$ m (Exp. 1). Fig. 5a reveals that for $R = 0$ the meandering crests oscillate in time and shift in the y-direction. Similar behavior of the crests is seen for $R = 1$ mm/yr before $t = 10$ ka (Fig. 5b), while afterwards, the oscillation of the crests ceases. In the case that $R = 1.875$ mm/yr (Fig. 5c), the crest lines maintain their initial orientation.

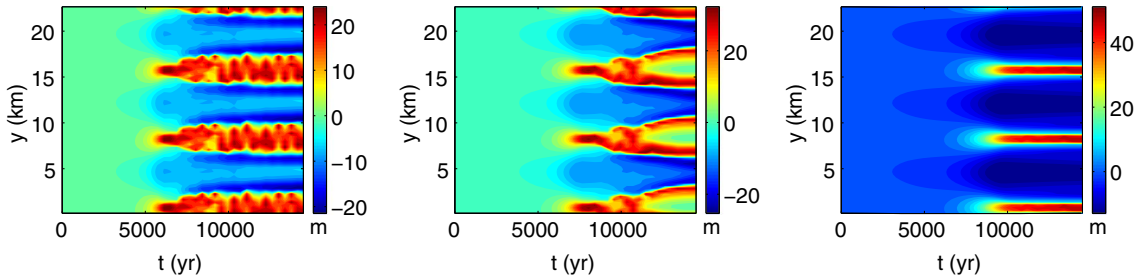

Fig. 5. Time evolution of the bed level along a transect at $x = 0.6$ km for different rates R of SLR with an initially undisturbed water depth $H_0 = 30$ m and $U = 0.75$ m/s (Exp. 1). (a) $R = 0$, (b) $R = 1$ mm/yr and (c) $R = 1.875$ mm/yr. The bed level obtained in the domain with $L_y = 7.5$ km is used to cover a domain with L_y that is 3 times larger. (For interpretation of the references to color in this figure legend, the reader is referred to the web version of this article.)

Fig. 6 presents, for several rates R of SLR in Exp. 1, the time evolution of the characteristics of the ridges, i.e., the root mean square height h_{rms}, the global growth rate Γ, crest level with respect to the mean sea level ($h_{cr} - H$) and relative ridge height h_{rel}. For a larger R, the global growth time τ_g and the root mean square height h_{rms} at time $t > \tau_g$ are larger, while the maximum global growth rate Γ is smaller. For $R = 3$ mm/yr, the global growth time has not been reached yet before the end of the simulation ($t = 15$ ka). In the cases that $R > 0$, the crest levels keep pace with the rising sea level, while the relative ridge height h_{rel} at time $t = \tau_g$ hardly changes ($h_{rel} \sim 90\%$).

3.2. Active ridges subject to SLR only: sensitivity behavior to H_0

Fig. 7 shows the time evolution of the bed level along a transect in the y-direction for different values of the initially undisturbed water depth H_0

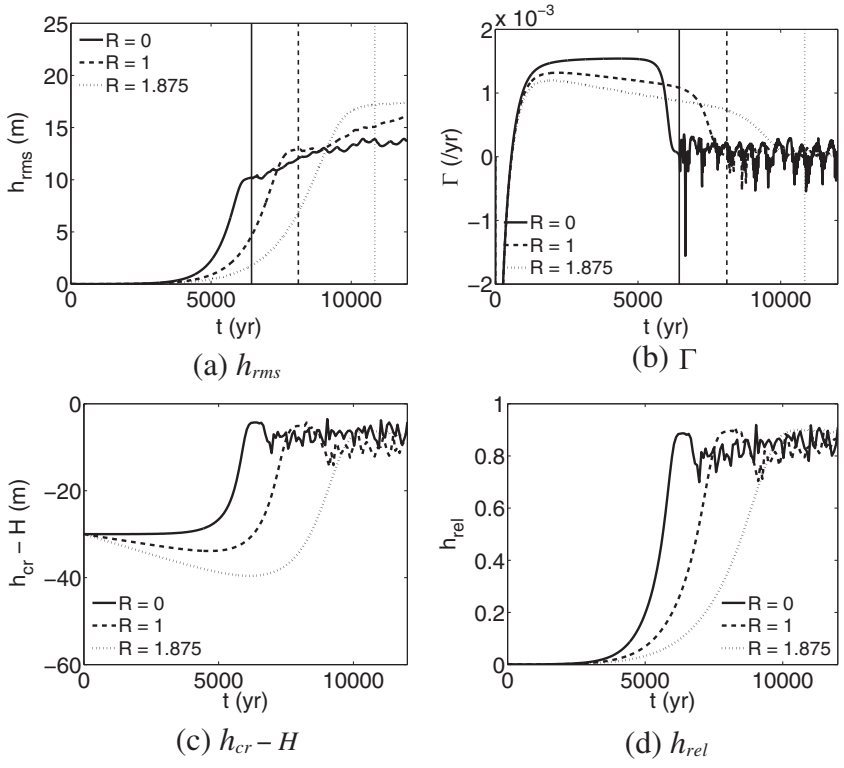

Fig. 6. Time evolution of (a) the root mean square height h_{rms}, (b) the global growth rate Γ, (c) crest level with respect to the mean sea level ($h_{cr} - H$), and (d) relative ridge height h_{rel} of the ridges for different rates R of SLR (unit: mm/yr) in Exp. 1 (using present-day values of H_0 and U for the Dutch Banks). (c) and (d) are related to the bed level along a transect at $x = 0.6$ km. The vertical lines indicate the global growth time.

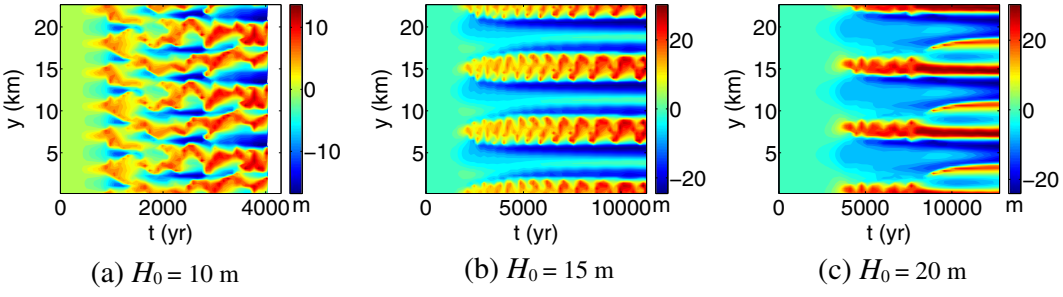

Fig. 7. As Fig. 5 but for different initially undisturbed water depth H_0 and a fixed rate of SLR $R = 1.875$ mm/yr (Exp. 2). (For interpretation of the references to color in this figure legend, the reader is referred to the web version of this article.)

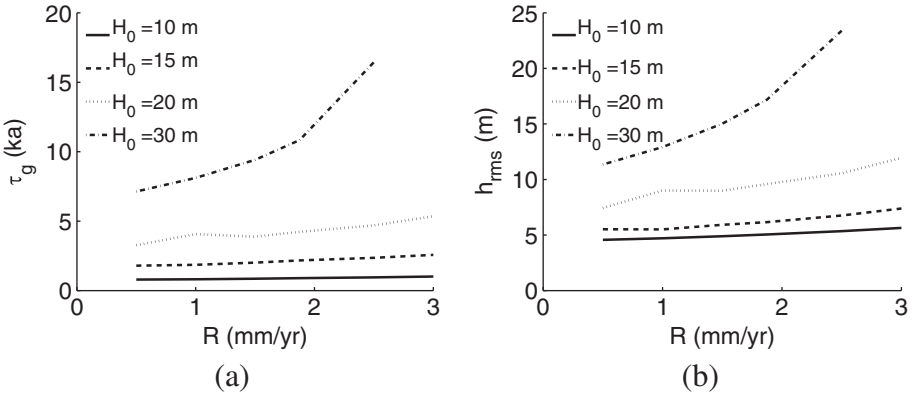

Fig. 8. (a) The global growth time τ_g and (b) the root mean square height h_{rms} at time $t = \tau_g$ against the rate of SLR for different water depths H_0 (Exp. 2). For comparison, the results for $H_0 = 30$ m (Exp. 1) are also presented.

with a constant rate of SLR $R = 1.875$ mm/yr. It is seen that the spacing of the initially preferred bedform for $H_0 = 10$ m is smaller than that for relatively large depths $H_0 = 15$, 20 m. In all the cases, tidal sand ridges with spatially meandering crests occur (not shown), and the crests oscillate in time after the exponential growth stage. For $H_0 = 20$ m, the oscillation of the crests lasts for approximately 5 ka, afterwards it ceases and the orientation and spacing of the ridges change (the latter is not shown, as is seen in middle panels of Fig. 4). Changes in the orientation and spacing of the ridges are also found for $H_0 = 15$ m with $R = 3$ mm/yr and $H_0 = 20$ m with $R = 2.5$, 3 mm/yr (not shown).

Fig. 8 shows the global growth time τ_g and the root mean square height h_{rms} at time $t = \tau_g$ against the rate of SLR for different initial water depths H_0 (Exp. 2). As H_0 increases from 10 m to 30 m, the global growth time τ_g and the root mean square height h_{rms} at time $t = \tau_g$ increase significantly. For instance, for $R = 1.875$ mm/yr, τ_g = 0.9, 2.2, 4.2, and 11.0 ka for H_0 = 10, 15, 20, and 30 m respectively, and h_{rms} at time $t = \tau_g$ increases from 5 m to 17 m.

3.3. Active ridges subject to SLR and tidal current variation

Based on the Holocene tidal conditions in the southern North Sea from van der Molen and de Swart (2001), variation in the velocity amplitude and the principal direction of the background tidal current is considered in Exp. 3 and Exp. 4, respectively. The rate of SLR is kept fixed at $R = 1.875$ mm/yr and the initially undisturbed water depth is 15 m. Compared to the results of Exp. 2 (using a constant $U = 0.75$ m/s, $H_0 = 15$ m and $R = 1.875$ mm/yr), the time evolution of h_{rms}, Γ, h_{cr} and h_{rel} is similar to that in Exp. 3 (using time-varying U) and Exp. 4 (not shown). The main difference in the results of Exps. 2–4 (using the same H_0 and R) is in the global growth time τ_g, i.e., τ_g is approximately 40% larger in Exps. 3–4 (using time-varying U) than that in Exp. 2. In addition, considering changes in the principal current direction (Exp. 4) results in sand ridges with a spacing of approximately 3.8 km all the time (not shown). In all the simulations of Exps. 3–4, except the one using a constant $U = 0.5$ m/s in Exp. 3, in the end meandering crests occur that oscillate in time. For the case of a constant $U = 0.5$ m/s in Exp. 3, the ridges grow quite slowly: h_{rms} is smaller than 1 m after a simulation time of 20 ka.

3.4. Quasi-active/inactive ridges due to SLR and tidal current variation

Using the conditions that mimic those for the Celtic Banks, Exp. 5 is conducted to investigate the transition of ridges from active to quasi-active/inactive. The sensitivity of the occurrence of quasi-active/inactive ridges to R, H_0, U and $\Delta\varphi$ is examined in Exps. 6–9, respectively. To determine if a ridge is active, quasi-active or inactive, sand transport on the ridge is a direct measure. Fig. 9a shows the time evolution of the

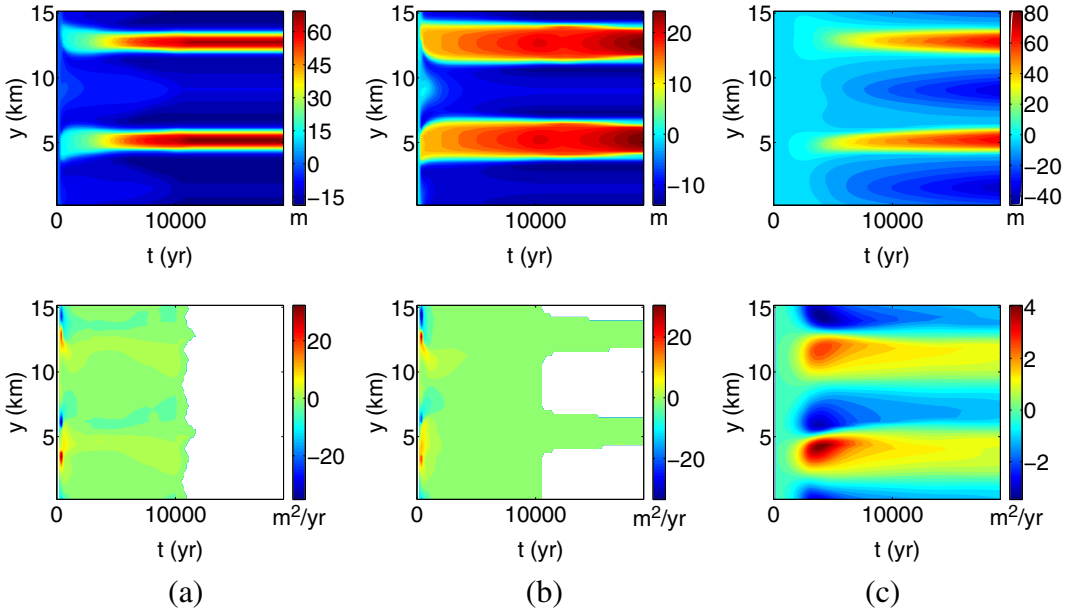

Fig. 9. Time evolution of the bed level h (top panels) and tidally averaged sand transport along a transect in the y-direction $\langle q_y \rangle$ (bottom panels) in (a) Exp. 5 (with time-varying R and U), (b) Exp. 6 (as Exp. 5 but with $R = 1$ mm/yr) and (c) Exp. 8 (as Exp. 5 but with $U = 0.67$ m/s). For $\langle q_y \rangle$, white color means $\langle q_y \rangle = 0$. (For interpretation of the references to color in this figure legend, the reader is referred to the web version of this article.)

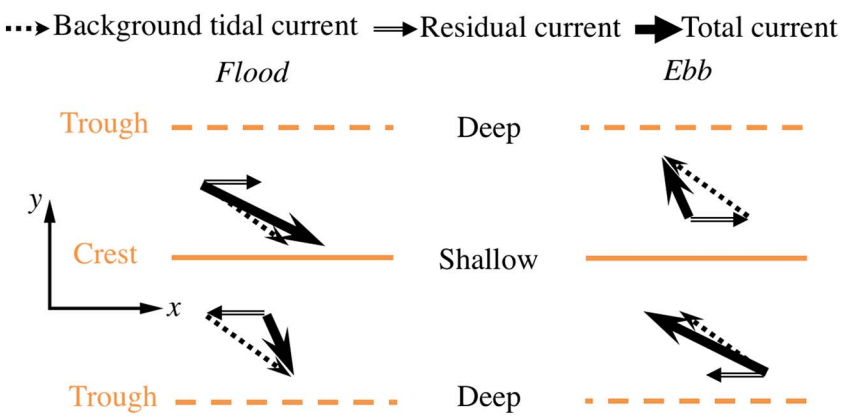

Fig. 10. Sketch of the background tidal current, residual current and total current over a bottom mode during flood and ebb in the Northern Hemisphere. The bottom mode is simplified as crest (solid) and trough (dash) lines.

bed level h and tidally averaged sand transport $\langle q_y \rangle$ along a transect in the y-direction for Exp. 5. Two ridges appear within the domain of 15 km long. At time $t \sim 10.5$ ka, $\langle q_y \rangle$ becomes 0 in the regions near the troughs, while it still changes near the crests, i.e., the ridges become quasi-active. After time $t \sim 11.5$ ka, in the whole domain $\langle q_y \rangle = 0$, i.e., the ridges turn inactive.

Quite similar results as those in Exp. 5 are found in Exp. 6 using a constant rate of SLR $R = 6.25$ mm/yr (not shown). Fig. 9b shows the time evolution of h and $\langle q_y \rangle$ in Exp. 6 using $R = 1$ mm/yr. Quasi-active ridges are observed but no inactive ridges occur. For $t \leq 20$ ka, the regions near the crests are always active ($\langle q_y \rangle \neq 0$), whereas the regions near the troughs turn inactive ($\langle q_y \rangle = 0$) at time $t \sim 10.5$ ka, and the area of the inactive regions increases as the sea level rises. This suggests that quasi-active ridges will turn inactive in the end, but in a much longer period compared to that in Exp. 6 using $R = 6.25$ mm/yr, in which inactive ridges are observed within 12 ka.

For different values of initially undisturbed water depth H_0 (Exp. 7), transition from active ridges to quasi-active and inactive ridges still occurs at similar times as those in Exp. 5. From Fig. 9c, which shows the time evolution of h and $\langle q_y \rangle$ in Exp. 8, it appears that if the variation of the velocity amplitude is not considered, before $t = 20$ ka the sandy bed is always active everywhere and the height of the ridges keeps increasing. Changes in the principal current direction (Exp. 9) do not affect the occurrence of quasi-active/inactive ridges.

4. Discussion

4.1. Meandering crests, rotated and non-rotated straight crests

The initial formation of tidal sand ridges has been explained by linear stability theory (Huthnance, 1982a). This concerns the study of the stability of a basic state, which is characterized by a spatially uniform background tidal current over a flat bottom, with respect to infinitesimal bottom perturbations. The latter are composed of Fourier modes (or bottom modes) that have an arbitrary wavelength and crest orientation with respect to the principal current direction. It was shown that for a strong tidal current (above 0.5 m/s), sand ridges form as a result of the joint action of the background tidal current and the residual current generated by tide-topography interactions. These results confirmed those of earlier qualitative studies by Zimmerman (1980, 1981) and Robinson (1981), in which it was demonstrated that a residual current is generated by torques due to bottom friction and Coriolis force around a ridge that is obliquely oriented with respect to the principal current direction. In addition, the strongest residual current is found if the ridge is cyclonically rotated with respect to the principal current direction. Fig. 10 shows a sketch of the background tidal current, the residual current and the total current over a bottom mode during flood and ebb. In that case, the residual current acts with the background tidal current upstream of the ridge while it acts against the current downstream. Consequently, sand transport upstream of the crests is larger than that downstream, and so net accumulation of sand occurs above the crests, and thus growth of the ridge. The stronger the residual current, the faster the height of the ridge grows, as was shown for the case of a rectilinear background tidal current by Hulscher et al. (1993). The intensity of the residual current is maximum if the spacing of the ridges is of the order of the tidal excursion length, i.e, the distance that water particles travel in a tidal period.

After some time from the beginning, the bottom mode of which the amplitude grows fastest (called the preferred mode/bedform) becomes dominant. This results in the presence of ridges of small heights with straight crests, as is seen in left panels of Fig. 4. Here it takes several thousands of years for the height of the ridges to become significant (in the order of meters), as the initial height of the perturbation is several centimeters and initially the perturbation grows exponentially with an e-folding time $1/\Gamma$ of several hundreds of years (from linear stability theory). Interestingly, for the chosen domain size for the Dutch Banks, the model results in Section 3 reveal that the behavior of the ridges in the end state depends on the initial water depth H_0 and the rate R of SLR. Three different types of behavior in the end state are observed (see Fig. 4, right panels), i.e., meandering crests that oscillate in time, and straight crests that are either rotated or non-rotated with respect to the crests of the initially preferred bedform (or the x-axis). Fig. 11 shows the presence of meandering crests, rotated and non-rotated straight crests in the end state for different values of R and H_0 (from Exps. 1–2 and additional experiments like Exp. 2 but $H_0 = 25$ m). It is seen that meandering crests occur for relatively small H_0, while non-rotated straight crests occur for relatively large H_0. For rotated straight crests, they are observed for small R with relatively large H_0 or relatively large R with intermediate H_0. Note that the values of H_0 for the occurrence of the ridges with meandering, rotated and non-rotated crests depend on

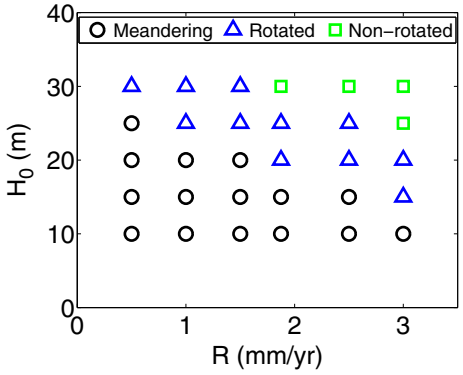

Fig. 11. Presence of meandering crests (circle), rotated (triangle) and non-rotated (square) straight crests with respect to the x-axis in the end state for different values of rate R of SLR and initially undisturbed water depth H_0, using the settings of the Dutch Banks (with constant wave conditions) and a domain of 7.5 km × 7.5 km.

choices of wave conditions. For a different wave climate, the values of H_0 for the transition between different types of behavior of the ridges will differ from those in Fig. 11.

Regarding meandering crests that oscillate in time, it was discussed in Yuan et al. (2017) that they are due to nonlinear interactions between the preferred bedform and bottom modes with crests normal/oblique to those of the preferred bedform. In particular, meandering crests occur if the domain length L_x is larger than the spacing of the initially preferred bedform λ_p, and the relative ridge height h_{rel} at the global growth time is above 80%. In relatively shallow waters (less than 50 m), the value of h_{rel} is inversely related to the amplitude of near-bed wave orbital velocity u_w, as stronger waves erode more sand at the crests. For the experiments setup, a larger L_x means that more bottom modes with crests normal/oblique to those of the initially preferred bedform are included in the domain.

Regarding the cases in which the end state is characterized by rotated straight crests with respect to the x-axis, it turns out that in the period before the end state, time-varying meandering crests occur. Moreover, the meandering crests show breaking behavior, i.e., a single crest breaks into two which are inclined with respect to the original crest (see middle panels of Fig. 4). The presence of meandering crests indicates that the amplitudes of bottom modes with crests normal/oblique to those of the initially preferred bedform become larger. The reason for this behavior is the following. If SLR is included, as the mean water depth H increases, the magnitude of the residual current generated by torques due to friction and Coriolis force decreases. This is because the frictional torque is proportional to H^{-2}, whereas the Coriolis torque, the additional torque related to quadratic bed shear stress and dissipation of residual vorticity are all proportional to H^{-1} (Zimmerman, 1980; Robinson, 1981). To check whether changes in the residual current occur in the model, Fig. 12 shows the residual current over the topography in Exp. 1 with a constant rate of SLR of 1 mm/yr at different simulation times. A decrease in the magnitude of the residual current after around 10 ka in that experiment is indeed observed. A weaker residual current gives rise to smaller growth rates of the bottom modes, and thus overall a smaller global growth rate or a larger global growth time. As changes in the amplitudes of the bottom modes become slower, the nonlinear interactions between the bottom modes also weaken, which is manifested as a decrease in the amplitude of the oscillation of the crests (distance that the crests shift in the y-direction). Consequently, the alternate breaking and merging behavior of the crests ceases. The dominant bottom mode determines whether in the end state the crests are oblique or parallel to those of the initially preferred bedform. In the cases of relatively large H_0 (above 30 m) and relatively large R (above 2 mm/yr) for the considered domain size in Exp. 1, the nonlinear interactions between the bottom modes are so weak such that no meandering crests occur at all.

4.2. Key for the transition from active to quasi-active/inactive ridges

For the settings of the Celtic Banks, in Exp. 5 active ridges become quasi-active at the simulation time $t \sim 10.5$ ka and subsequently inactive at $t \sim 11.5$ ka. Fig. 13a shows the time evolution of the amplitude U_e of the effective velocity calculated as $U_e = (U^2+0.5u_w^2)^{1/2}$, the critical velocity for sand erosion U_c and the amplitude of the near-bed wave orbital velocity u_w using the mean water depth H of Exp. 5. The time when U_e becomes smaller than U_c agrees with the time when the ridges become quasi-active/inactive. In contrast, in Exp. 6 for a relatively small constant rate of SLR (1 mm/yr), it takes much longer time for the ridges to become inactive. The reason is that by prescribing U in time, as H increases, U_c increases while u_w and U_e decrease (Fig. 13a), thus the time that U_e reaches U_c is shorter if H increases faster (larger R). For the setting of the Dutch Banks, the insert in Fig. 3 also indicates that if the tidal current amplitude is kept at 0.5 m/s, as the sea level rises, ridges will become quasi-active and inactive in the long term.

Note that as H increases, u_w approaches 0, which means that the amplitude U_e of the effective velocity is approximately equal to the tidal current amplitude U, and the change in U_c is minor (Figs. 3 and 13a). Thus if U is noticeably larger than U_c, the time for U_e to become smaller than U_c will be extremely long. As is seen in Fig. 9c ($U = 0.67$ m/s, $U_c \sim 0.5$ m/s), there is no sign that the ridges will turn quasi-active on the considered time scale.

The above observation reveals that if initially the velocity amplitude U of the tidal current is noticeably larger than the critical velocity for sand erosion U_c, the key for the transition from active to quasi-active ridges is a decrease in U such that U_e becomes less than U_c. If initially U

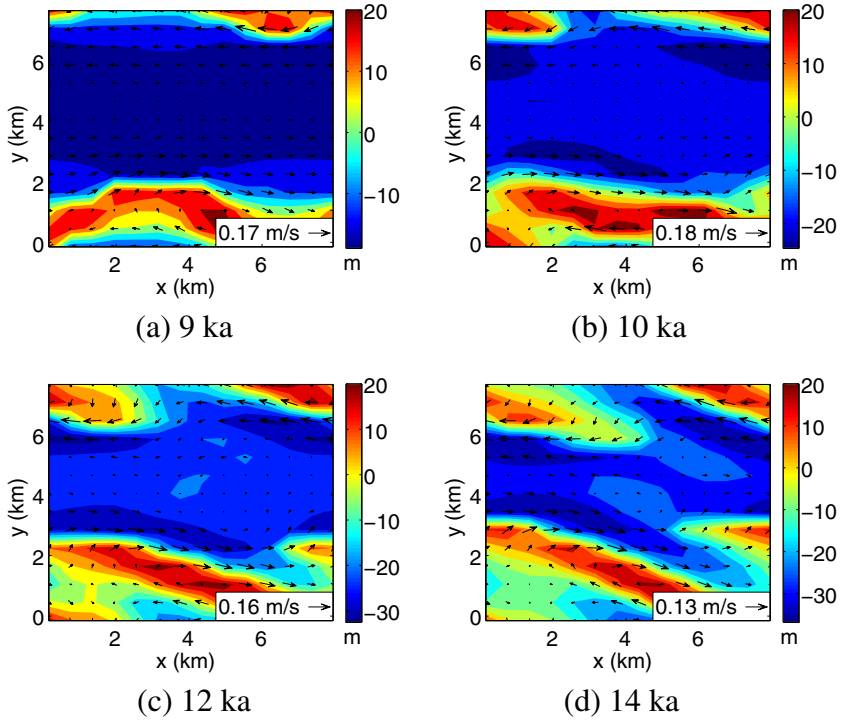

Fig. 12. The residual current (vectors) over the topography (color map) in Exp. 1 (using present-day values of H_0 and U for the Dutch Banks) with a constant rate of SLR of 1 mm/yr at different simulation times. The values in the white box indicate the maximum magnitude of the residual current. (For interpretation of the references to color in this figure legend, the reader is referred to the web version of this article.)

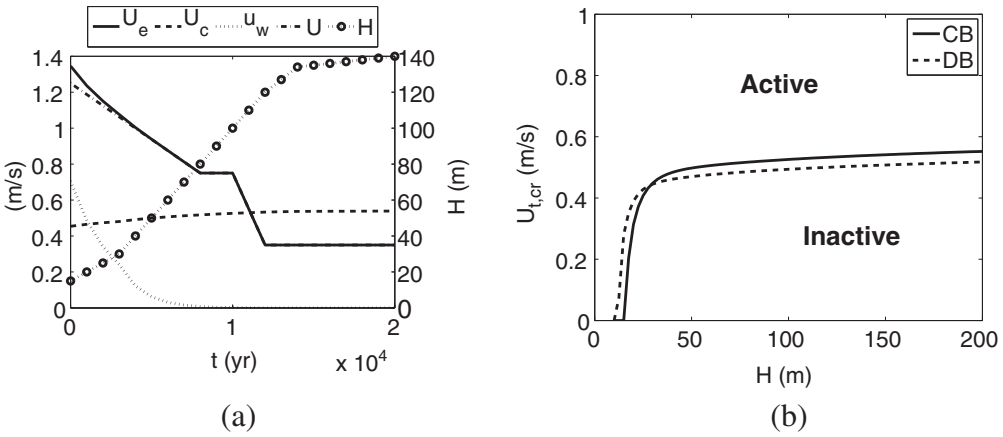

Fig. 13. (a) Time evolution of the amplitude U_e of the effective velocity calculated as $U_e = (U^2+0.5u_w^2)^{1/2}$ (solid line) for a prescribed tidal current amplitude U (dot–dashed line), the critical velocity for sand erosion U_c (dashed line) and the amplitude of near-bed wave orbital velocity u_w (dotted line), using the mean water depth H (dot–circle line). (b) Critical amplitude of tidal current $U_{t,cr} = (U_c^2-0.5u_w^2)^{1/2}$ that determines whether the sandy bed is active or inactive locally in different water depths H under a constant wave climate. The wave climate and the grain size for the Celtic Banks (CB, solid line) and the Dutch Banks (DB, dashed line) were employed.

is just above U_c, SLR alone will also give rise to quasi-active ridges. Further for quasi-active ridges to turn completely inactive, the associated time depends inversely on the rate of SLR (see Fig. 9a–b). Using the wave climate and the grain size for the Celtic Banks and the Dutch Banks, Fig. 13b shows the critical tidal current amplitude $U_{t,cr}$ calculated by $U_{t,cr} = (U_c^2-0.5u_w^2)^{1/2}$, which determines if the sandy bed in different water depths is active or inactive. It is seen from Fig. 13b that typically quasi-active/inactive ridges occur if U is below 0.5 m/s in a water depth above around 50 m, while active ridges occur in areas where U is above 0.5 m/s.

4.3. Sensitivity of the results to settings of the domain

In the previous sections, for the Dutch Banks the domain length in the y-direction L_y was chosen to be equal to the spacing of the initially preferred bedform ($\lambda_p = 7.5$ km) under the present-day condition, and L_x was set equal to L_y. For the Celtic Banks, a 1D configuration was used and L_y was chosen based on the observed spacing (15 km). Additional experiments were conducted to examine the sensitivity of the results of Exps. 1–5 to the domain length.

For Exp. 1, the experiment with the present-day setting $R = 1$ mm/yr, $H_0 = 30$ m, and $U = 0.75$ m/s was chosen as the reference case. First, L_y was fixed to 7.5 km and different values of L_x were used, i.e., $L_x = 3$, 4.5, 6, 9 km. Fig. 14a shows the root mean square height h_{rms} against time for different L_x. For the default setting ($L_y = L_x = 7.5$ km), the global growth time τ_g is 8.1 ka and h_{rms} at time τ_g is 12.9 m. For different values of L_x, the relative changes in τ_g and h_{rms} at time τ_g are within 12% and 4%, respectively. Fig. 15a–c shows the time evolution of the bed level along a transect at $x = 0.6$ km for different values of L_x. In all the cases, except the one in which $L_x = 3$ km, during the growth phase meandering crests occur that oscillate in time, and in the end state rotated straight crests are observed (not shown, similar to what is displayed in middle panels of Fig. 4). The reason that straight crests occur in the case $L_x = 3$ km is that L_x is smaller than λ_p, as was discussed in Section 4.1.

Next, different values of L_y were used. Integer multiples of λ_p were considered, such that the initially preferred bedform would fit in the domains, i.e., $L_y = 15$, 22.5 km ($L_x = 4.5$ km was chosen for reasons of computational efficiency). Fig. 14b shows the root mean square height h_{rms} against time for different L_y. Compared to the results using $L_x = 4.5$ km and $L_y = 7.5$ km, for different values of L_y, the relative changes in τ_g and h_{rms} at time τ_g are within 9% and 14%, respectively. Fig. 15d–f show the time evolution of the bed level along a transect at $x = 0.6$ km for different values of L_y. Changes in the orientation and spacing of the ridges still occur for $L_y = 15$ km (not shown). In the case of $L_y = 22.5$ km, two meandering crests together with a non-rotated straight crest (at $y \approx 4$ km) occur at the end of simulation time $t = 15$ ka (not shown). In all the cases with different values of L_x and L_y, the relative ridge height h_{rel} is approximately 90% at time $t = \tau_g$.

In Exps. 2–4, different initial values of undisturbed water depth H_0 and tidal current amplitude U were used, but the domain size was kept fixed. Thus, in these cases L_y was not equal to the wavelength of the initially preferred bedform. Linear stability analysis revealed that for $H_0 = 10$, 15, 20 m with $U = 0.75$ m/s (Exp. 2), the initially preferred bedform has a spacing of 3.9, 5.1 and 6.3 km, respectively, and for $H_0 = 15$ m with $U = 0.5$ m/s (Exps. 3 and 4), the initially preferred bedform has a spacing of 4.5 km. For the above conditions the crests are all 37 ± 1° cyclonically rotated with respect to the principal direction of the background tidal current. To examine the consequence of choosing a fixed L_y, additional simulations were carried out in which L_y was equal to the spacing of the initially preferred bedform λ_p. This was done for Exp. 2 using $R = 1.875$ mm/yr and Exps. 3–4 using time-varying U. The results were compared with those of Exps. 2–4 using $L_y = 7.5$ km and $R = 1.875$ mm/yr. The relative differences in τ_g and

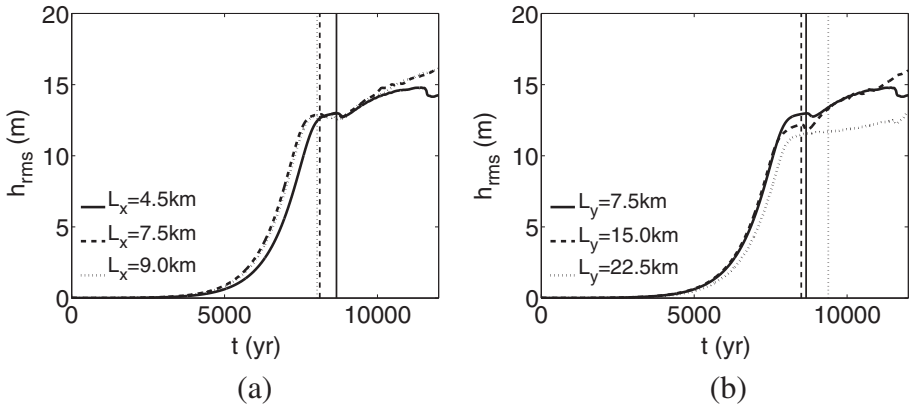

Fig. 14. As Fig. 6a but for sensitivity of the results of Exp. 1 using $R = 1$ mm/yr to (a) L_x ($L_y = 7.5$ km) and (b) L_y ($L_x = 4.5$ km).

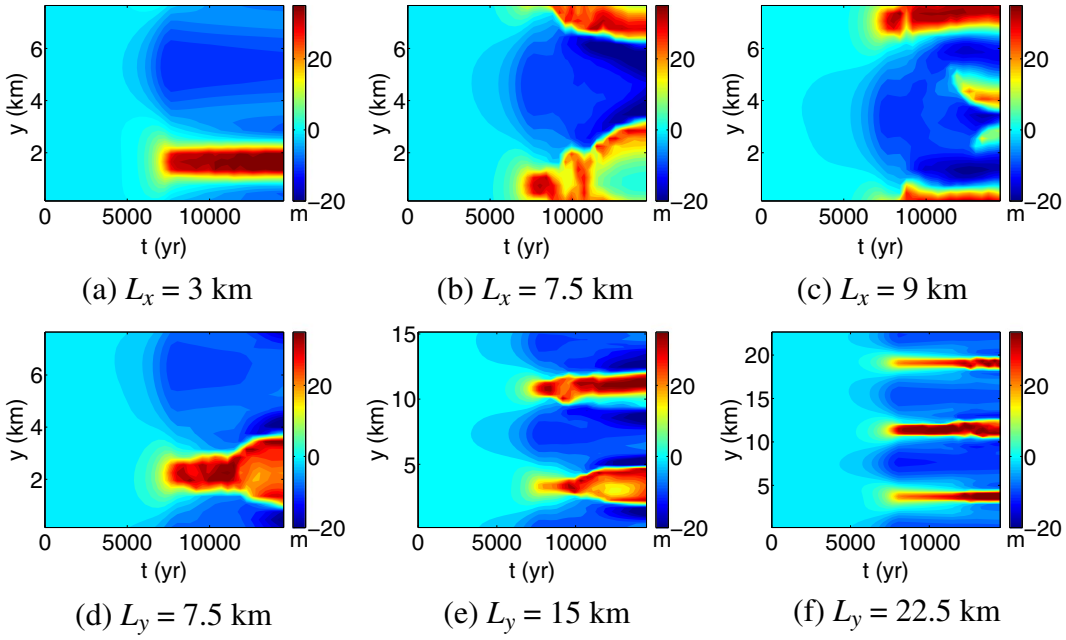

Fig. 15. As Fig. 5b but with no extension in the *y*-direction for (a)–(c) different length L_x (L_y = 7.5 km), (d)–(f) different length L_y (L_x = 4.5 km) in Exp. 1 using R = 1 mm/yr. Note the differences in scales in the plots d–f. (For interpretation of the references to color in this figure legend, the reader is referred to the web version of this article.)

h_{rms} at time τ_g are all within 20% and 18%, respectively. The features of meandering crests and rotated straight crests in the end state in the experiments using $L_y = \lambda_p$ are similar to those in the experiments using a fixed L_y of 7.5 km (not shown). Another difference for Exp. 4 using different L_y is that only one crest occurs in the domain with L_y = 4.5 km, while two crests occur in the domain with L_y = 7.5 km.

For Exp. 5, a larger domain with L_y = 30 km was used. Four ridges appear in the domain, with a spacing in the range of 5–10 km, and a height of 60–100 m. Similar to the results using L_y = 15 km, the ridges become quasi-active at simulation time $t \sim$ 10.5 ka and inactive at $t \sim$ 11.5 ka.

The above analysis reveals that if a larger domain is used, the behavior of the ridges differs from that in a smaller domain, especially if more bottom modes with crests normal/oblique to those of the initially preferred bedform are included (a larger L_x). The reason is that more nonlinear interactions occur by including more bottom modes. Nonetheless, using the above different domain sizes, the general characteristics (growth time, height, active/quasi-active/inactive status) of the ridges are similar.

Regarding the orientation of the domain (or the choice of the principal current direction), in this study the principal current direction was chosen such that the crests of the initially preferred bedform are parallel to the *x*-axis. For the range of values of the water depth and the tidal current amplitude used here, changes in the orientation of the initially preferred bedform are minor. Also, from the results of the experiments (Exps. 4 and 3 using U = 0.75 m/s from 2 ka, Exps. 5 and 9) which include/exclude changes in the principal current direction, it has been shown that the growth time and shape of the ridges in those experiments are similar. Based on the above considerations, it is expected that the influence of the domain orientation on the evolution of the ridges in this study will be small. Note that, due to constraints of the computational efficiency of the model, the analysis here has been limited to relative small variations in the domain size. It would be interesting to explore the effect of the domain size and the domain orientation together more extensively, but for that the efficiency of the model needs to be improved, possibly by using implicit numerical scheme or by using parallel computation.

4.4. Comparison between modeled and observed tidal sand ridges

In Roos et al. (2004), from Fourier analysis of the present-day seabed topography in the area of the Dutch Banks, the dominant spacing of tidal sand ridges in the area was shown to be in the range of 5.7–9.8 km, the height of the ridges is around 8 m and the relative ridge height is around 26%. The settings of Exp. 4 (Table 1) in the simulation period from t = 0 to t = 8 ka mimic the overall changes in the sea level and the tidal current in the area of the Dutch Banks from 8 ka BP to the present. The modeled ridges have a spacing of approximately 4 km, they reach their global growth time at t = 4 ka and their relative height is around 85% afterwards. At t = 8 ka, the height of the ridges is approximately 40 m.

The southeastern sand ridges in the Celtic Sea have a spacing of around 15 km and are 20–50 m high, the water depth above the crests is around 110 m (Belderson et al., 1986), and the relative height is 15%–31%. The settings of Exp. 5 (Table 1) represent the changes in the sea level and the tidal current during the last 20 ka for the Celtic Banks. For L_y = 15 km, the model yields a spacing of 7.5 km and the ridge height is 90 m (h_{rel} = 57%), and for L_y = 30 km, the modeled spacing is 5–10 km and the ridge height is between 60 and 100 m (h_{rel} = 38% –63%).

The differences in the spacing, the growth stage (before or after the global growth time) and the height between modeled and observed ridges are due to several reasons. Some of the reasons have already been discussed in Yuan et al. (2017), i.e., neglecting the vertical structure of the flow such that interactions between small- and large-scale bedforms are excluded, simplification in the composition of tidal constituents and the choice of a small domain size. In this study the tidal forcing is even simpler than that in Yuan et al. (2017), i.e., only the M_2 tide is considered here and no residual currents or overtides of M_2 are included. Besides these reasons, other reasons are discussed below.

First, the uncertainty in the amplitude U of the tidal current and the strong sensitivity of the ridge height to U contribute to those differences. For the Dutch Banks, compared to the case of a constant current amplitude of 0.75 m/s (Exp. 2 using H_0 = 15 m and R = 1.875 mm/yr), using a constant current amplitude of 0.5 m/s (Exp. 3) significantly slows down the growth of the ridges. In Exp. 3 (U = 0.5 m/s), at the

simulation time 8 ka the ridge height is less than 1 m (not shown). It is thus plausible that the observed Dutch Banks are still in the growth stage, while in the model setting of Exp. 4 the growth rate of the ridges was overestimated. The latter strongly depends on the chosen values of the tidal current amplitude U, the rate R of SLR and the initial water depth H_0. As is seen in Fig. 8a, the global growth time increases as R or H_0 increases, especially for the latter one.

Second, the formulation of the effective velocity $u_e = (|\vec{u}|^2+0.5u_w^2)^{1/2}$ follows that of Roos et al. (2004), whereas different expressions of u_e are present in other studies. For instance, the formulation of Soulsby-Van Rijn in Soulsby (1997) for u_e is $u_e = (|\vec{u}|^2+(0.009/C_d)u_w^2)^{1/2}$ for monochromatic waves, where C_d is the drag coefficient. It turns out that, using the latter formulation, the contribution of wave stirring to u_e, i.e., the coefficient in front of u_w^2, is approximately 9 times larger for a water depth of 15 m, which means a 3 times larger wave height in the latter case. Since u_w approaches 0 as the water depth increases (see e.g. Fig. 3), different formulations of u_e affect the evolution of sand ridges in shallow waters (less than 50 m). Using $u_e = (|\vec{u}|^2+(0.009/C_d)u_w^2)^{1/2}$ for Exps. 4 and 5, both the initially preferred bedforms have a spacing of 9.6 km, and compared to the results using $u_e = (|\vec{u}|^2+0.5u_w^2)^{1/2}$, their initial growth rates decrease, especially for the Dutch Banks (by approximately 60%).

Also, only bed load sand transport was considered in the present model; a modified formulation of Fredsøe and Deigaard (1992) was used and the coefficients in this formulation (including the bed slope coefficient Λ) were not tuned. Soulsby (1997) showed that using different formulations for bed load sand transport yields transports rates that vary by a factor of more than 4. Roos et al. (2004) found that, by using a formulations for suspended load transport instead of bed load transport or by increasing Λ, the value of h_{rel} became smaller in the end state. Whether sand transport is dominated by bed load or suspended load depends on the grain size of the sand and the intensity of the flow. On the considered time scale, in the field changes in the grain size of the sand occur. These changes, together with the changes in the sea level and the flow, will have implications for the mode of sand transport (bed load and suspended load). Furthermore, it was assumed that erodibility of the bottom was not obstructed by e.g. rocky structures. Limited availability of sand prevents the ridge height from keeping increasing, and thus it accelerates the process that active ridges turn quasi-active/inactive.

Finally, the wave conditions are assumed to be constant in time. In reality, wave heights and wave periods change on both large (decades and centuries) and small (days to months) time scales. Roos et al. (2004) showed that in waters with depths less than 50 m, as the amplitude of near-bed wave orbital velocity increases, the relative ridge height decreases. As was shown in Neill et al. (2009), the present-day peak annual significant wave height H_s (10–15 m) and peak annual peak wave period T_p (18–19 s) in the Celtic Sea are much larger than the annual root mean square values of H_s (3–4 m) and T_p (7–8 s), and the same applies to the southern North Sea. Houthuys et al. (1994) presented an example that showed the effect of short-term variation of wave conditions (due to storm) on tidal sand ridges. They observed that changes in the surface level of sand waves (rhythmic bedforms with a spacing in the order of 100 m) on top of the Middelkerke Bank in the southern North Sea reached up to 1.2 m after successive storms within 3 months.

Note that the bed shear stress (see Eq. (10) in Appendix B) is calculated using the tidal current alone, whereas waves also contribute to the bed shear stress. The effect of the additional contribution of wind waves to the bed shear stress is similar to an increase in the linear friction coefficient as in Roos et al. (2004), which results in a smaller spacing and a larger growth rate.

To summarize, there are quantitative differences between modeled and observed ridges, but the model results are highly sensitive to the chosen values of the parameters. Note that there are also many similarities between modeled and observed ridges. It is evident from Fig. 1 that meandering ridges as shown in Fig. 4 (model results) are observed in almost all areas where tidal sand ridges occur. Similar successive ridges, as seen in the middle right panel of Fig. 4 (model results), are observed in the area of Norfolk Banks (Hearty Knoll, Winterton Ridge, Hammond Knoll and Haisborough Sand, see Fig. 1a at around 53° N, 2° E) in the southern North Sea (Caston, 1972). The spacings between these observed ridges (especially Hearty Knoll, Winterton Ridge and Hammond Knoll, approximately 3.5 km) are smaller than those of the ridges observed further offshore. The model results, which show breaking behavior of crests and decreases in the spacing of the ridges under SLR, suggest that the formation of these observed successive ridges with relatively small spacings may be related to changes in the sea level. Also, the reason why active ridges become quasi-active shown in this study could explain the evolution of other offshore sand ridges, such as those in the eastern Yellow Sea (Park et al., 2006) and the East China Sea (Liu et al., 2007).

5. Conclusions

The dynamics of tidal sand ridges subject to changes in the sea level and tidal conditions in the long term are studied by using a nonlinear morphodynamic model. The focus has been on the sensitivity of the growth time and height of active ridges to SLR and tidal current variation, as well as on the reason why active ridges become quasi-active/inactive. Two basic settings have been examined, which mimic the situations of the Dutch Banks and the Celtic Banks.

Generally active tidal sand ridges occur if the velocity amplitude of the tidal current U is large (typically above 0.5 m/s). For active ridges, considering SLR makes the root mean square height h_{rms} of the ridges keep on increasing. For larger fixed rate of SLR, the global growth time τ_g becomes larger, so does h_{rms} at time $t = \tau_g$. For a smaller initial U, τ_g is larger. If variation in the principal current direction is accounted for, changes in the growth time and height of the ridges are minor. For the parameter setting used in this study, in a fixed domain, three types of behavior of active ridges in the end state are observed: meandering crests that oscillate in time, and straight crests that are either rotated or non-rotated with respect to the crests of the initially preferred bedform. The final behavior of the ridges depends on the initial conditions (depth, tidal current amplitude), changes in the sea level and tidal current amplitude and the number of bottom modes in the domain.

Within the considered time range (20 ka), assuming a constant wave climate (wave height and wave period), if initially the tidal current amplitude U is noticeably larger than the critical velocity for sand erosion U_c, a decrease in U such that U becomes approximately smaller than U_c plays a key role in the occurrence of quasi-active ridges. In the case that initially $U \sim U_c$, SLR alone will also give rise to quasi-active ridges. The time scale for quasi-active ridges to turn further inactive is inversely proportional to the rate of SLR. Modeled sand ridges qualitatively agree with observed sand ridges, but spacings are underestimated and heights are overestimated.

Acknowledgments

The first author is financially supported by the China Scholarship Council (No. 201206250029).

Appendix A

The depth-averaged shallow water equations are used to model the water motion:

$$\frac{\partial \widetilde{D}}{\partial t} + \nabla\cdot(\widetilde{D}\,\vec{u}) = 0, \tag{6}$$

$$\frac{\partial \vec{u}}{\partial t} + (\vec{u}\cdot\nabla)\vec{u} + f\vec{e_z}\times\vec{u} = -g\nabla\widetilde{\zeta} + \vec{F_p} - \frac{\vec{\tau_b}}{\rho\widetilde{D}}. \tag{7}$$

Here, $\widetilde{\zeta} = \zeta - \zeta_0$ is the surface elevation related to bottom undulations, where ζ is the free surface elevation, $\widetilde{D} = \widetilde{\zeta} + H - h$ is the water depth related to $\widetilde{\zeta}$. Vector $\vec{u}$ is the depth-averaged velocity, with u and v being its components in the x- and y-directions, respectively, and $\vec{\tau_b}$ is the bed shear stress vector.

The spatially uniform pressure gradient force $\vec{F_p}$, which drives a spatially uniform background tidal flow $\vec{u_0}$ in the absence of bottom undulations, obeys the momentum balance

$$\vec{F_p} = \frac{\partial \vec{u_0}}{\partial t} + f\vec{e_z}\times\vec{u_0} + \frac{\vec{\tau_{b0}}}{\rho H}, \qquad \text{with} \qquad \vec{F_p} \equiv -g\nabla\zeta_0. \tag{8}$$

Here, ζ_0 is the surface variation induced by $\vec{F_p}$ on a flat bottom, g is the gravitational acceleration, and $f = 2\Omega\sin\Phi$ is the Coriolis parameter, with Ω the angular frequency of the Earth and Φ the latitude. Furthermore, $\vec{e_z}$ is a unit vector in the vertical direction, ρ is the constant water density. For a given $\vec{u_0}$, $\vec{F_p}$ is determined by Eq. (8), as the bed shear stress vector $\vec{\tau_{b0}}$ is determined by $\vec{u_0}$ (for explicit formulation see Appendix B). The horizontal components u_0 and v_0 of $\vec{u_0}$ are specified as harmonic series,

$$u_0 = a\cos(\omega t - \phi)\cos\varphi - b\sin(\omega t - \phi)\sin\varphi, \tag{9a}$$

$$v_0 = a\cos(\omega t - \phi)\sin\varphi + b\sin(\omega t - \phi)\cos\varphi. \tag{9b}$$

In these expressions, ω and ϕ are the angular frequency and phase of a tidal constituent, a and b are the sizes of semi-major and semi-minor axes of the tidal ellipse, and φ is the angle between the major axis of the tidal ellipse and the x-axis. The ellipticity of the tidal constituent is defined as $\epsilon = b/a$.

Appendix B

The quadratic friction law is employed to evaluate the bed shear stress $\vec{\tau_b}$:

$$\vec{\tau_b} = \rho C_d|\vec{u}|\vec{u}, \qquad C_d = [2.5\ln(11\widetilde{D}/k_s)]^{-2}, \tag{10}$$

where C_d is the drag coefficient, and k_s is the Nikuradse roughness that measures the roughness of the sea bed. Following Soulsby and Whitehouse (2005), in the presence of ripples, k_s is related to the dimensionless grain size D_* by

$$k_s = 202\ d\ D_*^{-0.554}, \qquad D_* = \left[\frac{g(s-1)}{\nu^2}\right]^{1/3} d. \tag{11}$$

Here, s is the density ratio of sand and water, d is the median grain diameter, and ν is the kinematic viscosity of water.

For sand transport, the sand transport coefficient α_e is given by

$$\alpha_e = \frac{30}{\mu_d \pi C'^3}\frac{1}{(s-1)g}, \tag{12}$$

with

$$C' = 2.5\ln\left(\frac{11\widetilde{D}}{2.5d}\right), \tag{13}$$

where μ_d is the dynamic friction coefficient and C' is the grain-related conductance coefficient. The critical depth-averaged velocity for sand erosion U_c relates to the critical Shields parameter θ_c by

$$U_c = C'[(s-1)gd\theta_c]^{1/2}. \tag{14}$$

An empirical relation through the dimensionless grain size D_* (Soulsby, 1997) is used to calculate θ_c:

$$\theta_c = \frac{0.3}{1+1.2D_*} + 0.055[1-\exp(-0.02D_*)]. \tag{15}$$

To obtain the effective velocity u_e given by $u_e = (|\vec{u}|^2 + 0.5u_w^2)^{1/2}$, following Soulsby (2006), the amplitude of the depth-dependent wave-induced near-bed orbital velocity u_w is parameterized as

$$u_w = \frac{H_w}{2}\left(\frac{g}{\widetilde{D}}\right)^{\frac{1}{2}}\exp\left\{-\left[\frac{4.41}{T_w}\left(\frac{\widetilde{D}}{g}\right)^{\frac{1}{2}}\right]^{2.45}\right\}. \tag{16}$$

Here, H_w and T_w represent the wave height and wave period of a monochromatic wave, respectively. The reason to use Eq. (16) instead of the physical formulation of u_w from linear wave theory is that the physical formulation of u_w is an implicit function of water depth and iteration is required to obtain u_w.

Appendix C

An explicit finite-difference numerical scheme (Caballeria et al., 2002) is used to solve the system (Eqs. (1)–(3) and (8)–(16)). In space a central second-order discretization is applied, and in time an explicit fourth-order Runge-Kutta scheme is used. Moreover, a morphological acceleration factor β (Roelvink, 2006) is introduced into Eq. (1) (replace $\partial h/\partial t$ by $\partial h/\partial(\beta t)$) to accelerate the morphodynamic processes. Values of β in the range of 50–450 are used in this study. Generally for a small β, the simulation period is also small for reasons of computational efficiency.

Table 2
Default parameter values in the experiments.

Parameter	Value	Description
Φ	53° N/49° N	Latitude
ω_{M_2}	1.4×10^{-4} rad s^{-1}	Angular frequency of M_2 tide
g	9.81 m s^{-2}	Gravitational acceleration
Λ	2.0	Bed slope coefficient
p	0.4	Bed porosity
ν	1.4×10^{-6} m^2 s^{-1}	Kinematic viscosity of water
s	2.6	Density ratio between sand and water
d	0.25/0.4 mm	Grain size
μ_d	0.6	Dynamic friction coefficient
Δx	300 m	Grid size in the x-direction
Δy	300 m	Grid size in the y-direction
Δt	6–12 s	Time step

If two values (e.g. 0.25/0.4 mm) are listed, the first one refers to the Dutch Banks and the second one refers to the Celtic Banks.

Appendix D

Following Young and Verhagen (1996), the wave energy E relates to the water depth H, wind speed U_{10} at a height of 10 m above the water surface and fetch length F by

$$\frac{g^2E}{U_{10}^4} = 3.64 \times 10^{-3}\left[\tanh A_1 \tanh\left(\frac{B_1}{\tanh A_1}\right)\right]^{1.74}, \tag{1}$$

with

$$A_1 = 0.493\left(\frac{gH}{U_{10}^2}\right)^{0.75}, \qquad B_1 = 3.13 \times 10^{-3}\left(\frac{gF}{U_{10}^2}\right)^{0.57}. \tag{2}$$

The significant wave height H_s is thus calculated as $H_s = 4\sqrt{E}$. The peak wave period T_p is calculated from

$$\frac{U_{10}}{gT_p} = 0.133\left[\tanh A_2 \tanh\left(\frac{B_2}{\tanh A_2}\right)\right]^{-0.37}, \tag{3}$$

with

$$A_2 = 0.331\left(\frac{gH}{U_{10}^2}\right)^{1.01}, \qquad B_2 = 5.215 \times 10^{-4}\left(\frac{gF}{U_{10}^2}\right)^{0.73}. \tag{4}$$

To obtain the velocity amplitude of the background tidal current in a water depth close to 0, it is assumed that the pressure gradient force $\overrightarrow{F_p}$ remains constant in time for small water depths. Using Eq. (8) and applying Lorentz linearization of the bed shear stress (Zimmerman, 1982), the following equations for (u, v) on a flat bottom are derived

$$\frac{\partial u}{\partial t} - fv = F_{px} - \frac{rUu}{H}, \qquad \frac{\partial v}{\partial t} + fu = F_{py} - \frac{rUv}{H}. \tag{5}$$

Here, $r = \frac{8}{3\pi}C_dU$ is the linear friction coefficient, U is the velocity amplitude (a function of H), and F_{px} and F_{py} are the components of $\overrightarrow{F_p}$ in the x- and y-directions. Writing $(u,\ v,\ F_{px},\ F_{py}) = \Re\{(\hat{u},\ \hat{v},\ \hat{F}_{px},\ \hat{F}_{py})e^{-i\omega t}\}$, where $\Re$ means real part, $i = \sqrt{-1}$ and the symbol ^ indicates the complex amplitude, a system for the complex amplitudes of the flow $(\hat{u},\ \hat{v})$ is derived. From the assumption that $\overrightarrow{F_p}$ is constant in time and using the conditions at certain location, e.g. the area of the Dutch Banks ($H = 15$ m, $U = 0.5$ m/s and $\epsilon = -0.2$, as in Exp. 4), $(\hat{F}_{px},\ \hat{F}_{py})$ are calculated. Consequently, the system for $(\hat{u},\ \hat{v})$ is closed, and for any H, the velocity amplitude U is obtained.

Fig. 16a and b shows the significant wave height H_s and peak wave period T_p versus water depth H for a wide range of fetch length (5–200 km) and a constant wind climate $U_{10} = 8$ m/s that represent the wind climate in the North Sea (Grabemann and Weisse, 2008). It is seen that for H larger than 10 m, H_s and T_p can be assumed to be constant. Fig. 16c shows the amplitude U_e of the effective velocity $u_e = (|\vec{u}|^2 + 0.5u_w^2)^{1/2}$ versus H by using H_s and T_p in Fig. 16a and b as the wave height H_w and period T_w, and assuming that $\overrightarrow{F_p}$ is constant in time and is the same as that at 8 ka BP in the southern North Sea (see settings of Exp. 4). A critical water depth H_{0c} (below which no sand transport occurs) of approximately 10 m is found, which is not sensitive to the choice of H_s and T_p for that setting.

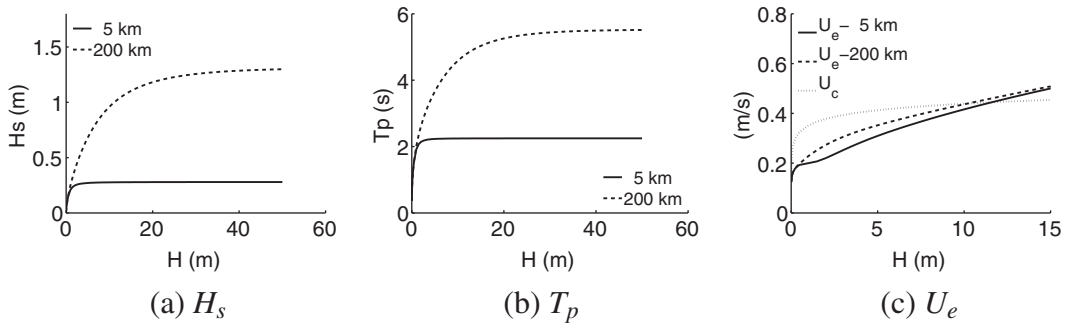

Fig. 16. (a) Significant wave height H_s and (b) peak wave period T_p versus water depth H for a range of fetch length (5–200 km, see legend) and a constant wind climate U_{10} = 8 m/s, calculated from Eqs. (1)–(4). (c) Amplitude U_e of the effective velocity $u_e = (|\vec{u}|^2+0.5u_w^2)^{1/2}$ and critical velocity for sand erosion U_c versus H, with u_w calculated from Eq. (16) using H_s and T_p in (a) and (b) as the wave height H_w and period T_w, and U obtained from the assumption that the pressure gradient force $\vec{F_p}$ is constant and the same as that at 8 ka BP in the southern North Sea (Exp. 4).

References

Beets, D.J.D.J., van der Spek, A.J.F.A.J.F., 2000. The Holocene evolution of the barrier and the back-barrier basins of Belgium and the Netherlands as a function of late Weichselian morphology, relative sea-level rise and sediment supply. Geol. Mijnb./Neth. J. Geosci. 79 (1), 3–16.

Behre, K.E.K.E., 2007. A new Holocene sea-level curve for the southern North Sea. Boreas 36, 82–102.

Belderson, R.H.R.H., Pingree, R.D.R.D., Griffiths, D.K.D.K., 1986. Low sea-level origin of Celtic Sea sand banks — evidence from numerical modelling of M_2 tidal streams. Mar. Geol. 73, 99–108.

Besio, G.G., Blondeaux, P.P., Vittori, G.G., 2006. On the formation of sand waves and sand banks. J. Fluid Mech. 557, 1–27.

Caballeria, M.M., Coco, G.G., Falqués, A.A., Huntley, D.A.D.A., 2002. Self-organization mechanisms for the formation of nearshore crescentic and transverse sand bars. J. Fluid Mech. 465, 379–410.

Caston, V.N.D.V.N.D., 1972. Linear sand banks in the southern North Sea. Sedimentology 18, 63–78.

Dyer, K.R.K.R., Huntley, D.A.D.A., 1999. The origin, classification and modelling of sand banks and ridges. Cont. Shelf Res. 19, 1285–1330.

Fleming, K.K., Johnston, P.P., Zwartz, D.D., Yokoyama, Y.Y., Lambeck, K.K., Chappell, J.J., 1998. Refining the eustatic sea-level curve since the Last Glacial Maximum using far- and intermediate-field sites. Earth Planet. Sci. Lett. 163, 327–342.

Fredsøe, J.J., Deigaard, R.R., 1992. Mechanics of Coastal Sediment Transport. World Scientific.

Garnier, R.R., Calvete, D.D., Falqués, A.A., Caballeria, M.M., 2006. Generation and nonlinear evolution of shore-oblique/transverse sand bars. J. Fluid Mech. 567, 327–360.

Grabemann, I.I., Weisse, R.R., 2008. Climate change impact on extreme wave conditions in the North Sea: an ensemble study. Ocean Dyn. 58 (3-4), 199–212.

Houthuys, R.R., Trentesaux, A.A., De Wolf, P.P., 1994. Storm influences on a tidal sandbank's surface (Middelkerke Bank, southern North Sea). Mar. Geol. 121 (1-2), 23–41.

Hulscher, S.J.M.H.S.J.M.H., de Swart, H.E.H.E., de Vriend, H.J.H.J., 1993. The generation of offshore tidal sand banks and sand waves. Cont. Shelf Res. 13 (11), 1183–1204.

Huthnance, J.M.J.M., 1982a. On one mechanism forming linear sand banks. Estuar. Coast. Shelf Sci. 14, 79–99.

Huthnance, J.M.J.M., 1982b. On the formation of sand banks of finite extent. Estuar. Coast. Shelf Sci. 15, 277–299.

Kenyon, N.H.N.H., Belderson, R.H.R.H., Stride, A.H.A.H., Johnson, M.A.M.A., 1981. Offshore tidal sand-banks as indicators of net sand transport and as potential deposits. Spec. Publ. Int. Assoc. Sedimentol. 5, 257–268.

Lambeck, K.K., 1995. Late Devensian and Holocene shorelines of the British Isles and North Sea from models of glacio-hydro-isostatic rebound. J. Geol. Soc. 152 (3), 437–448.

Liu, Z.Z., Berne, S.S., Saito, Y.Y., Yu, H.H., Trentesaux, A.A., Uehara, K.K., Yin, P.P., Liu, J.P.J.P., Li, C.C., Hu, G.G., Wang, X.X., 2007. Internal architecture and mobility of tidal sand ridges in the East China Sea. Cont. Shelf Res. 27 (13), 1820–1834.

Liu, Z.Z., Xia, D.D., Berne, S.S., Wang, K.K., Marsset, T.T., Tang, Y.Y., Bourillet, J.J., 1998. Tidal deposition systems of China's continental shelf, with special reference to the eastern Bohai Sea. Mar. Geol. 145, 225–253.

Neill, S.P.S.P., Scourse, J.D.J.D., Bigg, G.R.G.R., Uehara, K.K., 2009. Changes in wave climate over the northwest European shelf seas during the last 12,000 years. J. Geophys. Res. 114 (C06015). http://dx.doi.org/10.1029/2009JC005288.

Nnafie, A.A., de Swart, H.E.H.E., Calvete, D.D., Garnier, R.R., 2014. Effects of sea level rise on the formation and drowning of shoreface-connected sand ridges, a model study. Cont. Shelf Res. 80, 32–48.

Off, T.T., 1963. Rhythmic linear sand bodies caused by tidal currents. Bull. Am. Assoc. Pet. Geol. 47, 324–341.

Park, S.-C.S.-C., Lee, B.-H.B.-H., Han, H.-S.H.-S., Yoo, D.-G.D.-G., Lee, C.-W.C.-W., 2006. Late Quaternary stratigraphy and development of tidal sand ridges in the eastern Yellow Sea. J. Sediment. Res. 76 (9), 1093–1105.

Robinson, I.I., 1981. Tidal vorticity and residual circulation. Deep-Sea Res. 28A (3), 195–212.

Roelvink, J.A.J.A., 2006. Coastal morphodynamic evolution techniques. Coast. Eng. 53, 277–287.

Roos, P.C.P.C., Hulscher, S.J.M.H.S.J.M.H., Knaapen, M.A.F.M.A.F., 2004. The cross-sectional shape of tidal sandbanks: modelling and observation. J. Geophys. Res. 109 (F02003). http://dx.doi.org/10.1029/2003JF000070.

Scourse, J.J., Uehara, K.K., Wainwright, A.A., 2009. Celtic Sea linear tidal sand ridges, the Irish Sea Ice Stream and the Fleuve Manche: palaeotidal modelling of a transitional passive margin depositional system. Mar. Geol. 259 (1), 102–111.

Shennan, I.I., Bradley, S.S., Milne, G.G., Brooks, A.A., Bassett, S.S., Hamilton, S.S., 2006. Relative sea-level changes, glacial isostatic modelling and ice-sheet reconstructions from the British Isles since the Last Glacial Maximum. J. Quat. Sci. 21 (6), 585–599.

Soulsby, R.L.R.L., 1997. Dynamics of Marine Sands: A Manual for Practical Applications. Thomas Telford, London.

Soulsby, R.L.R.L., 2006. Simplified calculation of wave orbital velocities. Tech. Rep. TR-155. HR Wallingford Ltd.

Soulsby, R.L.R.L., Whitehouse, R.J.S.R.J.S., 2005. Prediction of Ripple Properties in Shelf Seas. Mark 2 Predictor for Time Evolution. Tech. Rep. TR155 Release 2.0. HR Wallingford Ltd., UK.

Stride, A.H.A.H., Belderson, R.H.R.H., Kenyon, N.H.N.H., Johnson, M.A.M.A., 1982. Offshore tidal deposits: sand sheet and sand bank facies. In: Stride, A.H.A.H. (Ed.), Offshore Tidal Sands: Processes and Deposits. Chapman and Hall, London, pp. 95–125.

Tambroni, N.N., Blondeaux, P.P., 2008. Sand banks of finite amplitude. J. Geophys. Res. 113 (C10028). http://dx.doi.org/10.1029/2007JC004658.

Uehara, K.K., Scourse, J.D.J.D., Horsburgh, K.J.K.J., Lambeck, K.K., Purcell, A.P.A.P., 2006. Tidal evolution of the northwest European shelf seas from the Last Glacial Maximum to the present. J. Geophys. Res. 111 (C09025). http://dx.doi.org/10.1029/2006JC003531.

van der Molen, J.J., de Swart, H.E.H.E., 2001. Holocene tidal conditions and tide-induced sand transport in the southern North Sea. J. Geophys. Res. 106 (C5), 9339–9362.

van Lancker, V.R.V.R., Bonne, W.W., Garel, E.E., Degrendele, K.K., Roche, M.M., den Eynde, D.V.D.V., Bellec, V.V., Brière, C.C., Collins, M.B.M.B., Velegrakis, A.F.A.F., 2010. Recommendations for the sustainable exploitation of tidal sandbanks. J. Coast. Res. 51, 151–164.

Yang, C.C., 1989. Active, moribund and buried tidal sand ridges in the East China Sea and the southern Yellow Sea. Mar. Geol. 88, 97–116.

Young, I.I., Verhagen, L.L., 1996. The growth of fetch limited waves in water of finite depth. Part 1. Total energy and peak frequency. Coast. Eng. 29 (1-2), 47–78.

Yuan, B.B., de Swart, H.E.H.E., Panadès, C.C., 2017. Modeling the finite-height behavior of offshore tidal sand ridges, a sensitivity study. Cont. Shelf Res. 137, 72–83.

Zimmerman, J.J., 1980. Vorticity transfer by tidal currents over an irregular topography. J. Mar. Res. 38 (4), 601–630.

Zimmerman, J.T.F.J.T.F., 1981. Dynamics, diffusion and geomorphological significance of tidal residual eddies. Nature 290 (5807), 549–555.

Zimmerman, J.T.F.J.T.F., 1982. On the Lorentz linearization of a quadratically damped forced oscillator. Phys. Lett. 89A (3), 123–124.